Optics Letters

Accurate 4Pi single-molecule localization using an experimental PSF model

Yiming Li,[1,2] Elena Buglakova,[2] Yongdeng Zhang,[3] Jervis Vermal Thevathasan,[2] Joerg Bewersdorf,[3,4] and Jonas Ries[2,*]

[1]Department of Biomedical Engineering, Southern University of Science and Technology, Shenzhen 518055, China
[2]EMBL, Cell Biology and Biophysics, Heidelberg 69117, Germany
[3]Department of Cell Biology, Yale School of Medicine, New Haven, Connecticut 06511, USA
[4]Department of Biomedical Engineering, Yale University, New Haven, Connecticut 06511, USA
*Corresponding author: jonas.ries@embl.de

Interferometric single-molecule localization microscopy (iPALM, 4Pi-SMS) uses multiphase interferometry to localize single fluorophores and achieves nanometer isotropic resolution in 3D. The current data analysis workflow, however, fails to reach the theoretical resolution limit due to the suboptimal localization algorithm. Here, we develop a method to fit an experimentally derived point spread function (PSF) model to the interference 4Pi-PSF. As the interference phase is not fixed with respect to the shape of the PSF, we decoupled the phase term in the model from the 3D position of the PSF. The fitter can reliably infer the interference period even without introducing astigmatism, reducing the complexity of the microscope. Using a spline-interpolated experimental PSF model and by fitting all phase images globally, we show on simulated data that we can achieve the theoretical limit of 3D resolution, the Cramér–Rao lower bound (CRLB), also for the 4Pi microscope.   © 2020 Optical Society of America

Single-molecule localization microscopy (SMLM, also known as PALM [1] or STORM [2]), has pushed optical resolution in microscopy toward the nanometer scale and has led to structural insights into cell biological questions [3–5]. 4Pi-SMLM (also called iPALM [6], 4Pi-SMS [7], or 4Pi-SMSN [8]) uses interference of the fluorescence signal detected with two opposing objective lenses to drastically increase the z resolution. Compared to the conventional single-objective 3D SMLM system [9–13], the dual-objective system collects twice as many photons. Overlaying both detection paths on a beam splitter results in self-interference of individual photons, provided the optical path length difference (OPD) is within the coherence length. Three [6] or four [7,8] interference phase images are then simultaneously recorded and provide a very sensitive read-out of a fluorophore's axial position (Fig. 1). The resulting axial resolution is about 6–10 times better than the axial resolution achievable with the single-objective system. In theory, 3D sub-10-nm resolution can be achieved with only 250 photons collected by each objective for an individual molecule [14].

In practice, however, this theoretical resolution limit has not been achieved in 4Pi SMLM, mainly due to suboptimal analysis approaches. This is in contrast to single-objective 3D SMLM, where the resolution limit can be practically reached by maximum likelihood estimation (MLE) using a bead-calibrated experimental point spread function (PSF) model [15].

The common method to extract the z position from the interference 4Pi-PSF is to determine the interference phase based on photometry between different interference channels [6–8]. However, this approach cannot extract information from the fringe pattern; thus, the localization accuracy is worse than the theoretical limit. Recently, spline-interpolated phase retrieved 4Pi-PSF models were introduced to fit the 4Pi-SMLM data [16]. While the method could potentially achieve the theoretical resolution, its usability in practice is limited. The problem is that the model fixes the phase with respect to the 3D position, whereas in real experiments the phase can easily drift, as even minor changes in temperature will change the OPD in the interference cavity. Thus, a simple multichannel 3D PSF is not well suited to describe real 4Pi-SMLM data.

To overcome these limitations, here we developed a new experimental PSF model that fully describes the 4D nature (x, y, z, and phase) of the 4Pi-PSF. The OPD between the two interference arms does not only depend on the axial position of the single molecule, but it is also affected by the path length of the interference cavity, which can change during the experiment. Therefore, we decouple the interference phase from the z position of the point emitter in our new 4Pi-PSF model. We then interpolate the phase-independent part of the experimental 4Pi-PSF model using cubic splines and globally fit the interference images from all phase channels. We show that we can achieve the theoretical limit of the 3D localization precision (Cramér–Rao lower bound, or CRLB) for 4Pi microscopy. Depending on the axial position, the achieved 3D localization precision is 1.8–20 times better than that achieved by the photometry-based localization method.

We represent the ideal 4Pi-PSF of a single emitter by coherently adding counterpropagating fields $E_1(x, y, z)$ and $E_2(x, y, z)$ from the upper and lower objectives, respectively [14]. By decoupling the interference phase φ from the
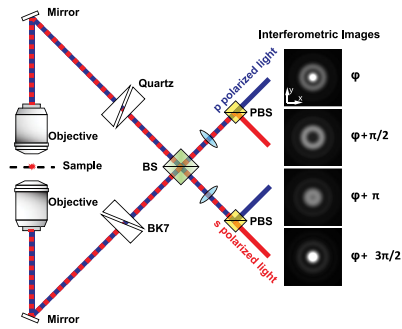
Fig. 1. Simplified schematic of a four-phase interference 4Pi-SMLM system. The emission fluorescence is collected by both objectives and interferes with itself at the beam splitter (BS). The phase shift between the p- and s-polarized channel is controlled by two modified Babinet–Soleil compensators (a phase shift of $\pi/2$ is shown). The p- and s-polarized light is separated by polarizing beam splitters (PBS) to create four interference images simultaneously.

two fields, the overall intensity of the coherent 4Pi-PSF can be written as

$$P(x, y, z, \varphi) = \left(E_1 + E_2 e^{-i\varphi}\right)\left(E_1 + E_2 e^{-i\varphi}\right)^*$$

$$= |E_1|^2 + |E_2|^2 + E_1 E_2^* e^{i\varphi} + E_1^* E_2 e^{-i\varphi}$$

$$= I + A\cos(\varphi) + B\sin(\varphi). \tag{1}$$

Here, $I(x, y, z) = |E_1|^2 + |E_2|^2$, $A(x, y, z) = 2(\mathrm{Re}(E_1)\mathrm{Re}(E_2) + \mathrm{Im}(E_1)\mathrm{Im}(E_2))$, and $B(x, y, z) = 2(\mathrm{Re}(E_1)\mathrm{Im}(E_2) - \mathrm{Im}(E_1)\mathrm{Re}(E_2))$ are slowly varying functions of x, y, z. They are real and the same for all four quadrants. Therefore, we can decompose the four-dimensional (4D) 4Pi-PSF into three phase-independent parts (I, A, and B), which can be approximated by slowly varying spline-interpolated volumetric image stacks, and modulated by the trigonometric functions that carry the phase.

We coin this model the IAB-based 4Pi-PSF model. A fit with this model (see below) results in the coordinates x, y, z and the interference phase φ. φ depends on the OPD of the two arms and thus on the precise z position of the fluorophore, but also has z-independent contributions φ_0 (refractive index change, interference cavity drift-induced OPD change, phase difference between quadrants, etc.), $\varphi = 2kz + \varphi_0$. Usually, φ_0 is slowly varying in time and similar for neighboring localizations, and it causes an apparent sample z drift, which we correct by a custom algorithm based on redundant cross correlation [15]. The z position calculated from the interference phase can be written as $z_\varphi = \varphi/2k$. Here, the wavenumber $k = 2n\pi/\lambda$ and n is the refractive index of the immersion medium. It is worth noting that z_φ calculated from the interference phase is much more precise than the z parameter within the I, A, B matrices, which corresponds to the distance of the point emitter to the focal plane of the objective. Therefore, we use z_φ for the final reconstruction of the super-resolution image.

In order to determine the 4D 4Pi-PSF experimentally, we need to determine the three 3D matrices I, A, and B. They can be calculated from three experimental 4Pi-PSFs with known interference phase [Fig. 2(a)] to solve for the three unknown
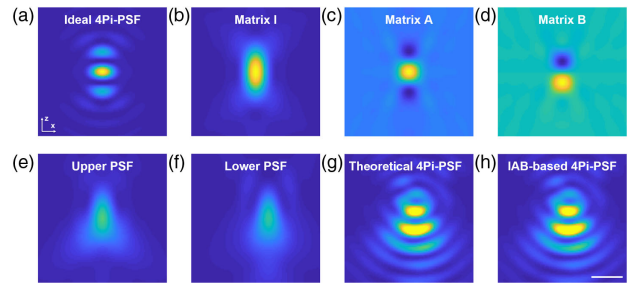

Fig. 2. IAB-based 4Pi-PSF model. (a) Ideal fully coherent 4Pi-PSF with interference phase of 0; (b) cross section of matrix I; (c) of A; (d) of B. (e) Upper objective PSF with astigmatism (100 mλ) and spherical (50 mλ) aberrations. (f) Lower objective PSF with astigmatism (-100 mλ) and shifted in x by 200 nm. (g) The theoretical 4Pi-PSF contains both coherent and incoherent parts (ratio α is 0.2). (h) IAB-based 4Pi-PSF calculated using Eq. (1). A full vectorial PSF model [17] was used for simulations with parameters: NA 1.35. Refractive index 1.40 (immersion medium and sample) and 1.518 (cover glass). Emission wavelength 668 nm. The same parameters are used throughout this work unless noted otherwise. Scale bar 500 nm.

parameters. Since the matrix I is the sum of the intensity of the upper and lower single-objective PSF, it can be easily obtained as a direct sum of single-objective PSFs [Fig. 2(b)]. Therefore, we actually only need two through-focus scans of 4Pi-PSFs with known interference phase (phase shift other than π) to calculate the remaining two 3D matrices. By solving two linear equations, we can obtain A and B [Figs. 2(c) and 2(d)],

$$A = (F(\varphi_1)\sin(\varphi_2) - F(\varphi_2)\sin(\varphi_1))/\sin(\varphi_2 - \varphi_1), \tag{2}$$

$$B = (-F(\varphi_1)\cos(\varphi_2) + F(\varphi_2)\cos(\varphi_1))/\sin(\varphi_2 - \varphi_1). \tag{3}$$

Here, $F(\varphi_1) = P(\varphi = \varphi_1) - I$, $F(\varphi_2) = P(\varphi = \varphi_2) - I$. φ_1 and φ_2 are the two interference phases of the two 4Pi-PSFs. Since different interference phase channels are usually acquired simultaneously in 4Pi-SMLM, it is easy to obtain two 4Pi-PSFs with different phases just by scanning the 4Pi-PSF in 3D once. In practice, we averaged many through-focus scans of bright fluorescent beads with the same phase to get high signal-to-noise data. The 3D matrices I, A, and B were calculated based on this averaged PSF.

During the derivation of our new IAB-based 4Pi-PSF model, we did not use approximations; thus, it can accurately describe even imperfect PSFs in the presence of aberrations. We validated this by simulations using a full vectorial model to calculate the single-objective PSFs [17], with different aberrations for upper and lower objectives, misalignment (lateral shift between PSFs), and astigmatism [Figs. 2(e) and 2(f)], which is often introduced to distinguish z positions at different interference periods ("phase unwrapping") [8,18]. Furthermore, in order to be close to a realistic 4Pi-PSF, we added up the counterpropagating electrical fields from the upper and lower objectives partially coherently and incoherently [16],

$$P_t(x, y, z, \varphi) = P(x, y, z, \varphi) + \alpha I(x, y, z). \tag{4}$$

Here, $\alpha \geq 0$ is the ratio between the incoherent part and the coherent part of the electrical field. The matrix I was calculated as in Eq. (1). We then chose a phase of $\varphi = 2\pi/3$, which is different from the phases used to calculate I, A, and B ($\varphi_1 = 0$,

$\varphi_2 = \pi/2$) and compared it with the theoretical 4Pi-PSF with the same phase [Figs. 2(g) and 2(h)]. As expected, these two PSFs are identical within machine precision.

In 4Pi-SMLM experiments, three or four phases with relative phase shifts of ϕ_i are detected simultaneously. The imaging model of the multichannel 4Pi-PSF is given as $\mu_{ki}(x, y) = \theta_{bi} + \theta_N/2 * P(x - \theta_x, y - \theta_y, \theta_z, \theta_\varphi + \phi_i)$. Here, μ_{ki} is the expected intensity value of pixel k at position (x, y) in channel i and is assumed to follow Poisson statistics due to the random nature of photon detection. For each channel, θ_{bi} are the background photons per pixel and assumed to be constant over the extent of the PSF. θ_N is the number of photons detected in each objective. θ_x, θ_y, and θ_z are the x, y, and z positions of the emitter. θ_φ is the interference phase. P is described as in Eq. (1). The objective function for MLE across different channels is given by $\chi^2_{\mathrm{mle}} =$

$$2\left(\sum_i \sum_k (\mu_{ki} - M_{ki}) - \sum_i \sum_{k, M_{ki} > 0} M_{ki} \ln(\mu_{ki}/M_{ki}) \right).$$ Here,

M_{ki} is the measured number of photons in the kth pixel in the ith channel. Similar to a previous implementation [19], we used a modified Levenberg–Marquardt algorithm for the nonlinear optimization process. We used cubic spline interpolation to interpolate the 3D matrices I, A, and B [15,20]. Since the interference phase is decoupled from the θ_z in the IAB-based 4Pi-PSF model, it is simple to calculate the partial derivatives along each parameter. We then used the fitted θ_z for phase unwrapping to estimate the period, which we added to θ_φ to get the absolute phase to calculate z_φ.

For fitting of the parameters globally across different channels, the spatial transformation between different channels can be calibrated using beads on cover glass. The phase shifts ϕ_i between different channels can be precisely determined as they directly follow the design of the interference cavity. θ_z is also considered to be identical for all channels as the calibration at different z positions is performed simultaneously for all channels. Based on whether a parameter is independent in each channel or the same in all channels, the Hessian and Jacobian matrices are constructed by using the information in one channel or across multiple channels [21]. We implemented the algorithm on the GPU and reached a fitting speed of 1617 molecules/s on a consumer graphic card (NVIDIA GTX 1070) for a fitting region of 13×13 pixels, while the fitting speed on the CPU (Intel Core i7-5930) was 268 molecules/s.

We then investigated the accuracy of our fitting approach on simulated data and compared it to the photometry-based method, as well as the CRLB. The CRLB was evaluated as the diagonal element of the inverse of the Fisher information matrix (Fig. 3). For photometry, we followed the work by Aquino and coworkers using the moment-based estimator [7]. The x and y positions were first obtained by fitting the summed image of all channels with a Gaussian model. As the central location of the molecule is known, the zeroth moment intensities were calculated by a weighted least squares fitting of a Gaussian with the amplitude being the only fitting parameter. The interference phase was analytically solved using the intensities under the assumption that they follow two sine models with a known phase shift between p- and s-polarized channels.

Our analysis [Figs. 3(a)–3(c)] reveals that the localization precision using MLE with our IAB-based 4Pi-PSF model can reach the CRLB in all dimensions. The localization precision for the photometry-based method is worse than the CRLB, specially for
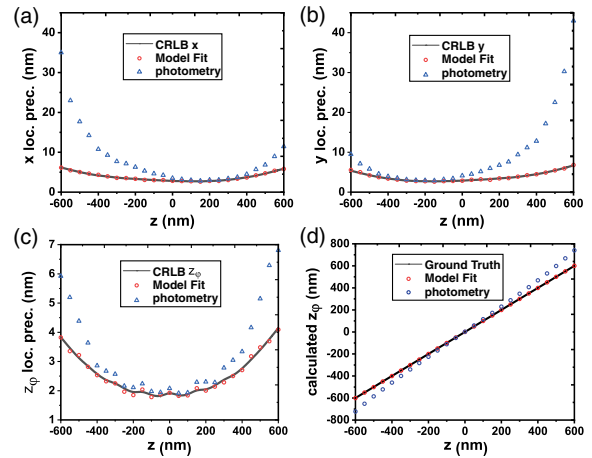

Fig. 3. Comparison of localization precisions and accuracies using the IAB-based 4Pi-PSF model fit and the photometry-based analysis method. Localization precision in, (a) x; (b) y; (c) z. Comparison of the returned z_φ and the ground truth z (d). 1000 4Pi single molecule images were simulated at each z position with four phase channels (0, $\pi/2$, π, $3\pi/2$) with an astigmatism of 100 mλ. For each objective, 2000 photons/localization and 20 background photons/pixel were used. The localization precision is calculated as the standard deviation.

molecules away from the focal plane. In x and y, the improvement from using the new model is up to fourfold [Figs. 3(a) and 3(b)]. The reason is that the model fit extracts information from the fringes in the interference PSF, whereas the summed PSF, which is used for lateral localization in photometry, does not contain these spatial features. The localization precision in z (standard deviation) is up to ~ 1.5 fold worse [Fig. 3(c)]. The large systematic errors for z localizations in photometry [Fig. 3(d)] indicate that the simple sinusoid model cannot fully describe the zeroth moment intensities, possibly due to the spherical wavefront captured by the high NA objective.

As even an unmodified (nonastigmatic) 4Pi-PSF has a different shape in different interference periods [7], we hypothesized that we can distinguish these interference periods directly using our 4Pi-PSF model fit. This would render the introduction of astigmatism obsolete, greatly simplifying the design of the microscope. To test our hypothesis, we simulated upper and lower objectives PSFs without introducing any aberration and coherently added them to produce an ideal 4Pi-PSF. In order to overcome the problem that the fitter might not converge across interference periods, we explored the bidirectional fitting approach as described before [15]. Here, we fit each single molecule twice with different starting z parameters (± 300 nm) and phases (0 and π). We then chose the solution of these two fits with the maximum likelihood. Similar to the 4Pi-PSF with astigmatism, we also could achieve the CRLB in all directions for the unaberrated 4Pi-PSF (Fig. 4).

To demonstrate that our approach works on real experimental 4Pi-SMLM data, we imaged nuclear pore complexes using a 4Pi microscope with a design based on Huang and coworkers [8]. Nuclear pore complexes are well suited as reference standards as they position the proteins at defined 3D locations in the cell [22]. We used genome edited cell lines in which we labeled Nup96-SNAP with BG-AF647 and embedded the sample in a refractive index matched buffer ($n = 1.40$, 38% 2,2'-thiodiethanol in standard glucose oxidase/catalase/MEA
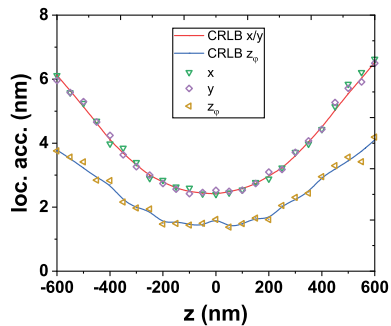
Fig. 4. Localization accuracy of unaberrated 4Pi-PSF: x, y, and z_φ localization accuracy of an ideal 4Pi-PSF without additional astigmatism. 1000 4Pi single molecule images were simulated at each z position with four phase channels (0, $\pi/2$, π, $3\pi/2$). For each objective, 2000 photons/localization and 20 background photons/pixel were used.
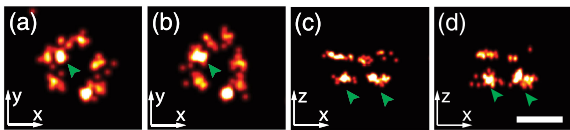

Fig. 5. Experimental data on nuclear pore complex. Nup96-SNAP-Alexa647 was imaged and reconstructed by (a) and (c), IAB-based 4Pi-PSF model and, (b) and (d), photometry-based method. (a) and (b), top view; (c) and (d), side view. Scale bar 100 nm.

buffer [15]). The two rings of Nup96 are clearly resolved in the axial dimension (Fig. 5). The clusters reconstructed by our model fit are smaller than those from photometry, both in $x−y$ [Figs. 5(a) and 5(b)] and $x−z$ [Figs. 5(c) and 5(d)], as indicated by the green arrow.

In conclusion, we developed a new 4Pi-PSF model to fully describe the 4D nature of the 4Pi-PSF. We decoupled the interference phase from the 3D position of the PSF and represent the 4Pi-PSF with three 3D matrices (I, A, and B) in combination with a simple phase term. Therefore, instead of calibrating a complete 4D 4Pi-PSF, we could obtain an experimental 4Pi-PSF just by calibrating the three 3D matrices, which is practically much easier. Furthermore, we developed a complete analysis pipeline to analyze the multiphase 4Pi-PSFs simultaneously. Our global fitter achieved the theoretical minimum uncertainty, the CRLB, in all dimensions. Compared to the conventional photometry-based approach, it greatly improved the localization precision and accuracy, enabling sub-10-nm resolution in all three dimensions even for rather dim single molecule conditions (2000 photons/molecule and 20 background/pixel). Moreover, the IAB-based 4Pi-PSF model fit allowed us to unwrap the phase without introducing additional aberrations that are usually used to distinguish different interference periods, which could simplify the design of 4Pi-SMLM microscopes. Finally, we validated our 4Pi-PSF model by imaging the biological samples, nuclear pore complex protein Nup96, and clearly resolved the double-ring structure with a distance of only 50 nm. We believe that this work is an important step in reaching the full potential of 4Pi-SMLM.

REFERENCES

1. E. Betzig, G. H. Patterson, R. Sougrat, O. W. Lindwasser, S. Olenych, J. S. Bonifacino, M. W. Davidson, J. Lippincott-Schwartz, and H. F. Hess, Science **313**, 1642 (2006).
2. M. J. Rust, M. Bates, and X. W. Zhuang, Nat. Methods **3**, 793 (2006).
3. M. Mund, J. A. van der Beek, J. Deschamps, S. Dmitrieff, P. Hoess, J. L. Monster, A. Picco, F. Nédélec, M. Kaksonen, and J. Ries, Cell **174**, 884 (2018).
4. A. Szymborska, A. de Marco, N. Daigle, V. C. Cordes, J. A. G. Briggs, and J. Ellenberg, Science **341**, 655 (2013).
5. K. Xu, G. Zhong, and X. W. Zhuang, Science **339**, 452 (2013).
6. G. Shtengel, J. A. Galbraith, C. G. Galbraith, J. Lippincott-Schwartz, J. M. Gillette, S. Manley, R. Sougrat, C. M. Waterman, P. Kanchanawong, M. W. Davidson, R. D. Fetter, and H. F. Hess, Proc. Natl. Acad. Sci. USA **106**, 3125 (2009).
7. D. Aquino, A. Schönle, C. Geisler, C. V. Middendorff, C. A. Wurm, Y. Okamura, T. Lang, S. W. Hell, and A. Egner, Nat. Methods **8**, 353 (2011).
8. F. Huang, G. Sirinakis, E. S. Allgeyer, L. K. Schroeder, W. C. Duim, E. B. Kromann, T. Phan, F. E. Rivera-Molina, J. R. Myers, I. Irnov, M. Lessard, Y. Zhang, M. A. Handel, C. Jacobs-Wagner, C. P. Lusk, J. E. Rothman, D. Toomre, M. J. Booth, and J. Bewersdorf, Cell **166**, 1028 (2016).
9. B. Huang, W. Wang, M. Bates, and X. W. Zhuang, Science **319**, 810 (2008).
10. S. R. P. Pavani, M. A. Thompson, J. S. Biteen, S. J. Lord, N. Liu, R. J. Twieg, R. Piestun, and W. E. Moerner, Proc. Natl. Acad. Sci. USA **106**, 2995 (2009).
11. D. Baddeley, M. B. Cannell, and C. Soeller, Nano Res. **4**, 589 (2011).
12. Y. Shechtman, S. J. Sahl, A. S. Backer, and W. E. Moerner, Phys. Rev. Lett. **113**, 133902 (2014).
13. M. F. Juette, T. J. Gould, M. D. Lessard, M. J. Mlodzianoski, B. S. Nagpure, B. T. Bennett, S. T. Hess, and J. Bewersdorf, Nat. Methods **5**, 527 (2008).
14. C. von Middendorff, A. Egner, C. Geisler, S. W. Hell, and A. Schönle, Opt. Express **16**, 20774 (2008).
15. Y. Li, M. Mund, P. Hoess, J. Deschamps, U. Matti, B. Nijmeijer, V. J. Sabinina, J. Ellenberg, I. Schoen, and J. Ries, Nat. Methods **15**, 367 (2018).
16. S. Liu and F. Huang, Commun. Biol. **3**, 220 (2020).
17. S. Stallinga and B. Rieger, Opt. Express **18**, 24461 (2010).
18. T. A. Brown, A. N. Tkachuk, G. Shtengel, B. G. Kopek, D. F. Bogenhagen, H. F. Hess, and D. A. Clayton, Mol. Cell. Biol. **31**, 4994 (2011).
19. T. A. Laurence and B. A. Chromy, Nat. Methods **7**, 338 (2010).
20. H. P. Babcock and X. W. Zhuang, Sci. Rep. **7**, 552 (2017).
21. S. Wolter, A. Löschberger, T. Holm, S. Aufmkolk, M.-C. Dabauvalle, S. van de Linde, and M. Sauer, Nat. Methods **9**, 1040 (2012).
22. J. V. Thevathasan, M. Kahnwald, K. Cieśliński, P. Hoess, S. K. Peneti, M. Reitberger, D. Heid, K. C. Kasuba, S. J. Hoerner, Y. Li, Y. Le Wu, M. Mund, U. Matti, P. M. Pereira, R. Henriques, B. Nijmeijer, M. Kueblbeck, V. J. Sabinina, J. Ellenberg, and J. Ries, Nat. Methods **16**, 1045 (2019).